Comp. Part. Mech. (2017) 4:119–130
DOI 10.1007/s40571-016-0132-5

Continuum modeling of rate-dependent granular flows in SPH

Ryan C. Hurley[1,2] · **José E. Andrade**[1]

Received: 23 May 2016 / Revised: 26 July 2016 / Accepted: 1 September 2016 / Published online: 13 September 2016

Abstract We discuss a constitutive law for modeling rate-dependent granular flows that has been implemented in smoothed particle hydrodynamics (SPH). We model granular materials using a viscoplastic constitutive law that produces a Drucker–Prager-like yield condition in the limit of vanishing flow. A friction law for non-steady flows, incorporating rate-dependence and dilation, is derived and implemented within the constitutive law. We compare our SPH simulations with experimental data, demonstrating that they can capture both steady and non-steady dynamic flow behavior, notably including transient column collapse profiles. This technique may therefore be attractive for modeling the time-dependent evolution of natural and industrial flows.

Keywords Granular media · Particulate flow · Smoothed particle hydrodynamics

1 Introduction

Many natural and industrial processes involve flow of granular media such as soils, sands, powders, and pulverized brittle materials. Examples of such processes include landslides, debris flows, bulk food transport, and ballistic impact of ceramics. These processes typically involve large deformations from a reference state and flow rates that vary from quasi-static to dynamic. Numerical models that can accurately simulate these flow features are essential as predictive tools. However, the lack of well-established rheological relations spanning flow-rate regimes has historically limited the development of such models.

Dry granular materials exhibit solid-like, liquid-like, or gas-like behavior depending upon their environment and excitation [1]. Numerical and experimental studies have established basic constitutive laws for a variety of geometries [2–5] and flow-rate regimes, from quasi-static [6,7] to rapid [3]. Jop and colleagues [5] proposed a constitutive law for steady-state granular flows that captures behavior across these regimes and in a variety of configurations [4,8]. To date, this constitutive law provides the most unifying framework for granular flows and has been adopted for modeling both steady and non-steady processes such as impact cratering and granular column collapse [9,10].

Mesh-free methods have recently gained popularity for modeling granular materials. Several authors [11,12] have used the material-point-method (MPM) to model granular flows, demonstrating the ability of this technique, with appropriate constitutive laws, to capture a wide range of flow-rate regimes. Others [13–15] have employed SPH for granular materials, capturing both quasi-static and dynamic regimes with models ranging from classical plasticity to fluid-like viscoplasticity. Viscoplastic formulations have also been used with the finite-element method [16] for modeling granular column collapse.

In this paper, we employ a simple viscoplastic constitutive law to simulate steady-state and non-steady granular flow behavior in a variety of geometries. We adopt the viscoplastic stress tensor proposed by [5] and use continuum energy balance to derive a non-steady dilatancy term. We implement the resulting constitutive law in Smoothed Particle Hydrodynamics (SPH) and test it in 3D dynamic scenarios to illustrate that the method captures both steady and non-steady granular flow behavior. Most notably, the method captures the

✉ Ryan C. Hurley
hurley10@llnl.gov

[1] Division of Engineering and Applied Sciences, California Institute of Technology, Pasadena, CA 91125, USA

[2] Present Address: Lawrence Livermore National Laboratory, Livermore, CA 94550, USA

transient profiles of a collapsing 3D granular column as well as scaling laws for final heights and lengths. Because the present paper tests the proposed constitutive framework in a variety of challenging flow environments, the technique may be attractive for modeling the full time-dependent evolution of geophysical and industrial flows in the future.

The layout of this paper is as follows. Section 2 outlines the balance and constitutive laws used to model granular materials. Section 3 discusses the SPH framework and the algorithm implemented in simulations. Section 4 presents three examples that demonstrate the ability of the method to model rate-dependent flows down inclined planes, capture column collapse scaling, and predict the non-steady dynamic structure of flows down inclined planes. Section 5 offers a discussion of future work and concluding remarks.

2 Balance and constitutive laws

This section details the balance and constitutive laws used to model granular materials.

2.1 Balance laws

The governing balance law we solve is the equation of momentum balance given by

$$\nabla \cdot \boldsymbol{\sigma} + \rho \boldsymbol{b} = \rho \boldsymbol{a}, \tag{1}$$

where $\boldsymbol{\sigma}$ is the Cauchy stress tensor, ρ is density, $\boldsymbol{b}$ is a body force, and $\boldsymbol{a}$ is material acceleration.

2.2 Constitutive law

We adopt a viscoplastic stress tensor used in [5] for steady-state modeling of granular flows

$$\boldsymbol{\sigma} = -p\boldsymbol{I} + \frac{(\mu p + c)\boldsymbol{D}}{|\boldsymbol{D}|}, \tag{2}$$

where p is pressure, $\boldsymbol{I}$ is the identity tensor, μ is friction, c is cohesion, $\boldsymbol{D} = \nabla \boldsymbol{v} + (\nabla \boldsymbol{v})^T$ is the strain rate tensor, and $|\boldsymbol{D}| = (\frac{1}{2}\boldsymbol{D} : \boldsymbol{D})^{1/2}$ is the second invariant of the strain rate tensor. The second term in Eq. (2) can be identified as the shear stress $\boldsymbol{\tau}$. While the effective viscosity, $(\mu p + c)/|\boldsymbol{D}|$ diverges in the quasi-static limit, we avoid singularities by using $|\boldsymbol{D}| + \epsilon$ in numerical calculations, where ϵ is a small parameter described below. Following the discussion in [5], a material having this stress tensor only flows in accordance with a Drucker–Prager-like yield condition when

$$|\boldsymbol{\tau}| > \mu_s p + c, \tag{3}$$

where μ_s is a coefficient of static yield.

We adopt an equation of state relating the pressure p to the density ρ in the granular material. This equation of state takes the form [17]

$$p = \begin{cases} \kappa \left[\left(\frac{\rho}{\rho_0} \right)^{\gamma} - 1 \right] & \rho \geq \rho_0 \\ 0 & \rho < \rho_0, \end{cases} \tag{4}$$

where ρ_0 is the loosest packing density of the granular material, and κ and γ are parameters that can be chosen to ensure an appropriate bulk modulus and scaling of p with ρ. For example, we choose $\gamma = 3/2$ in this paper to ensure a pressure–density relationship consistent with that found at the jamming transition for granular solids in [18]. Parameter κ is then constrained by the desired bulk modulus for the material through the relationship

$$K = \rho \frac{\mathrm{d}p}{\mathrm{d}\rho} = \begin{cases} \frac{3}{2}\kappa \left(\frac{\rho}{\rho_0} \right)^{3/2} & \rho \geq \rho_0 \\ 0 & \rho < \rho_0. \end{cases} \tag{5}$$

We note that introducing weak compressibility, in an addition to being necessary for determining the stress field in the material, also significantly reduces pressure oscillations that would otherwise occur near static conditions (e.g., also see [15]).

We next derive a friction law for the evolution of μ during steady-state and non-steady flow. The derivation mirrors that of classical stress–dilatancy relationships [6] and friction laws for non-steady granular shear flows [19]. Considering a granular material undergoing deformation at a rate $\boldsymbol{D}$, energy balance requires that

$$\rho \dot{e} = \frac{1}{2}\boldsymbol{\sigma} : \boldsymbol{D} - \nabla \cdot \boldsymbol{q} + \rho s, \tag{6}$$

where e is specific internal energy, $\boldsymbol{q}$ is heat flux, s is the rate of energy generation or decay by sources and sinks. The factor of $\frac{1}{2}$ in Eq. (6) accounts for the difference between the definition of $\boldsymbol{D}$ in [5] and the classical definition. The strain rate tensor can be decomposed into volumetric and deviatoric components as

$$\boldsymbol{D} = \frac{\mathrm{tr}(\boldsymbol{D})}{3}\boldsymbol{I} + \boldsymbol{D}_s, \tag{7}$$

where $\boldsymbol{D}_s = \boldsymbol{D} - \mathrm{tr}(\boldsymbol{D})\boldsymbol{I}/3$. Substituting Eqs. (2, 7) into Eq. (6), noting that $\boldsymbol{D} : \boldsymbol{I} = \mathrm{tr}(\boldsymbol{D})$, and solving for μ yields

$$\mu = \frac{\rho \dot{e} + \nabla \cdot \boldsymbol{q}}{p|\boldsymbol{D}|} - \frac{\rho s}{p|\boldsymbol{D}|} + \frac{\frac{1}{2}\mathrm{tr}(\boldsymbol{D})}{|\boldsymbol{D}|}. \tag{8}$$

During steady-state flow, granular materials are observed to deform at constant volume [5,6] and time-averaged internal energy, making the first and third term in Eq. (8) equal to zero. At steady-state, $-s$ is therefore the rate of steady-state energy dissipation and the term $-\rho s/(p|\boldsymbol{D}|)$ can be interpreted as the steady-state friction coefficient μ_{ss}. The

steady-state friction coefficient depends on strain rate, evolving from a static value μ_s at low strain rates to a peak value μ_p at the highest strain rates. In our model, we therefore adopt an empirical form for μ_{ss}, given by [7]

$$\mu_{ss} = \mu_s + \frac{\mu_p - \mu_s}{D^*/|\boldsymbol{D}| + 1}, \tag{9}$$

where D^* represents the scale of rate-strengthening. The steady-state friction can be rate-strengthening or rate-weakening depending upon the values of μ_s and μ_p, but is typically observed to be rate-strengthening in dry granular flows [2,4,5]. The friction law can be seen as a simplification of the one proposed in [5], in which $\boldsymbol{D}$ is replaced by the inertial number I and a pressure term is therefore incorporated into the equation. We choose to ignore pressure and use $\boldsymbol{D}$ since it, or mean velocity, is frequently used in the granular flow and flash-weakening literature with favorable results [7,20]. We also find favorable results in the present paper, suggesting that the variables contained in Eq. (9) are sufficient for the class of problems that we simulate. We also use $\boldsymbol{D}$ because, despite smoothing of the pressure field by the introduction of weak compressibility in Eq. (4), we still expect some spurious oscillations near quasi-static conditions that may affect the pressure field, and therefore I. Indeed, these oscillations in particle motion are responsible for the creeping flow observed when the material is in an apparently quasi-static state (noted in Sect. 3.3 and also in [15] using a similar model). We discuss extensions of classical SPH that may alleviate these oscillations in Sect. 5.

The third term in Eq. (8) is a form of dilation rate [21] which we denote β. We adopt the modified version

$$\beta = \frac{\frac{1}{2}\mathrm{tr}(\boldsymbol{D})}{|\boldsymbol{D}|}\frac{|\boldsymbol{D}|}{\eta}\exp\left(1 - \frac{|\boldsymbol{D}|}{\eta}\right), \tag{10}$$

where η represents a scale of dilatancy decay with strain rate (analogous to the model used in [7], where dilatancy rate decays with shear strain). This modified form for β ensures recovery of $\mu = \mu_{ss}$ at critical state and steady-state, as expected, and again avoids any effects of spurious oscillations in the velocity field. We use $\eta = 0.35\mathrm{s}^{-1}$ in the examples throughout this paper and discuss other values in Sect. 5. We restrict β to the range $0 \leq \beta \leq \mu_{ss}$. The upper bound on β is often found when enforcing non-negative plastic dissipation for Drucker–Prager-like plasticity laws. The lower bound reflects values used by [7] and may be relaxed to $-\mu_{ss}$ in the future.

We ignore the first term in Eq. (8) in the present work, assuming with insight from past work [19] that it is only relevant for faster flows than those considered here. The full friction coefficient considered in this work is therefore

$$\mu = \mu_{ss} + \beta, \tag{11}$$

and is consistent with those forms widely used in soil mechanics and other work [6–8,21]. This form allows us to capture the rate and dilation-dependent nature of granular materials across a range of flow rates.

3 Smoothed particle hydrodynamics

This section briefly describes SPH and its use for implementing the constitutive laws presented in this paper.

3.1 Background and kernel function

SPH is a mesh-free numerical method that uses Lagrangian particles of fixed mass to represent fixed mass regions of a physical material. In this paper, SPH particles represent fixed masses of granular media (not individual granular particles). SPH particles move according to integration of the governing balance, Eq. (1), and constitutive laws, Eq. (2). They retain field quantities, such as density and stress, representing those of the granular material at their location. Field quantities are computed by a summation interpolant employing a kernel function W with smoothing length h [22]. We use the classic cubic spline kernel in all summation interpolants [23]

$$W(r,h) = \frac{1}{h^3\pi}\begin{cases} 1 - \frac{3}{2}q^2 + \frac{3}{4}q^3 & 0 \leq q < 1 \\ \frac{1}{4}(2-q)^3 & 1 \leq q < 2 \\ 0 & q \geq 2, \end{cases} \tag{12}$$

where $q = r/h$ and $r = |\boldsymbol{x}_a - \boldsymbol{x}_b|$ is the distance between SPH particles labeled a and b, as shown in Fig. 1a. Some alternative kernels, including the spiky and double-humped cubic varieties, have been tested but do not demonstrate superior results for the examples presented here. Furthermore, Monaghan [22] has noted that no kernel shows significantly better results than the cubic spline for a wide range of problems. The smoothing length h is chosen as 1.2 times initial particle spacing [22], although similar results are found when h is 1.5 times initial particle spacing. The smoothing length is held constant during all simulations. Evolving the smoothing length with density is common in SPH simulations but is only necessary in simulations of highly compressible gases (e.g., see [24]); the granular materials modeled here do not undergo significant density changes for $\rho > \rho_0$ that would require smoothing length evolution.

Several monographs describe SPH in detail [22,25]. Here, we merely state that classical SPH has a number of attractive properties as a numerical method, including zero intrinsic dissipation, exact conservation of mass, momentum, energy,

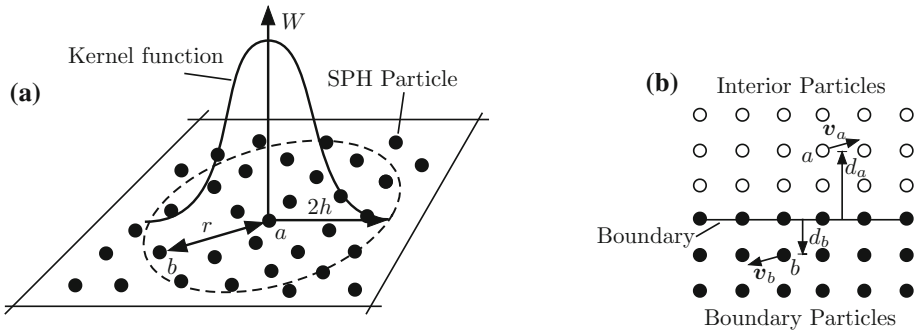

Fig. 1 **a** Cartoon of SPH cubic spline and lengths r and h. **b** Illustration of artificial boundary particle velocities

and entropy. In the present paper, SPH also allows us to easily capture large deformation and material fragmentation without expensive remeshing or mesh-refinement procedures required in grid-based approaches. All simulations are performed in a modified version of LAMMPS [26] and therefore benefit from that code's MPI architecture for parallel computing and periodic boundary conditions.

3.2 Density

Density is computed using the basic SPH equation with a Shepard filter applied at each time step. For a particle a, we first compute

$$\bar{\rho}_a = \sum_{b \in N} m_b W(r, h) \tag{13}$$

where m_b is the mass of SPH particle b and N is the set of neighbors of particle a. We then apply the Shepard filter [22] to obtain

$$\rho_a = \frac{\bar{\rho}_a}{\sum_{b \in N} \frac{m_b}{\bar{\rho}_a} W(r, h)}. \tag{14}$$

This filter corrects particle deficiencies near free surfaces and boundaries. We note that we have also employed the more common free surface density formulation proposed in [17] with nearly identical results to those presented in this paper.

3.3 Equation of motion

To update SPH particle locations, we evaluate Eq. (1) using SPH interpolants for each particle

$$\boldsymbol{a}_a = \rho_a \sum_{b \in N} \left(\frac{\boldsymbol{\sigma}_a}{\rho_a^2} + \frac{\boldsymbol{\sigma}_b}{\rho_b^2} + \Pi_{ab} \boldsymbol{I} \right) \cdot \nabla W(r, h) + \boldsymbol{b} \tag{15}$$

where $\boldsymbol{\sigma}$ is given by Eq. (2) and Π_{ab} is an artificial viscosity discussed below. In evaluating $\boldsymbol{\sigma}$ in Eq. (2), the strain rate tensor $D_a = \nabla \boldsymbol{v}_a + (\nabla \boldsymbol{v}_a)^T$ must be calculated using

$$\nabla \boldsymbol{v}_a = \sum_{b \in N} \frac{m_b}{\rho_b} (\boldsymbol{v}_b - \boldsymbol{v}_a) \otimes \nabla W(r, h). \tag{16}$$

The value of p_a used in $\boldsymbol{\sigma}_a$ is obtained from applying the equation of state (4) directly to the density ρ_a computed using Eq. (14). The value of μ used in $\boldsymbol{\sigma}_a$ is computed from Eq. (11), using $\boldsymbol{D}_a$. As noted previously, to avoid a singularity in Eq. (2), we use $|\boldsymbol{D}| + \epsilon$, where $\epsilon = 0.01h^2$ is a small number, rather than $|\boldsymbol{D}|$ in the denominator. As in [15], we also observe grain motion once an apparent quasi-static condition is reached. However, this grain motion is several orders of magnitude slower than that found during dynamic conditions (e.g., those during column collapse in Sects. 4.2, 4.3). Future extensions discussed in Sect. 5 may be able to alleviate any spurious oscillations that cause grain motion in the quasi-static limit.

The artificial viscosity Π_{ab} in Eq. (15) is commonly adopted to avoid spurious oscillations around shock fronts in hydrodynamic simulations [27] and is used in other SPH simulations of granular media [15]. We adopt [15,27]

$$\Pi_{ab} = -\alpha \frac{h \bar{c}_{ab}}{\bar{\rho}_{ab}} \frac{\boldsymbol{v}_{ab} \cdot \boldsymbol{r}_{ab}}{r^2}, \tag{17}$$

where α is a dimensionless parameter set to 0.004 throughout this paper, $\bar{c}_{ab}$ is the average sound speed at particles a and b, $\bar{\rho}_{ab}$ is the average density of particles a and b, $\boldsymbol{v}_{ab} = \boldsymbol{v}_a - \boldsymbol{v}_b$, and $\boldsymbol{r}_{ab} = \boldsymbol{r}_a - \boldsymbol{r}_b$. The wave speed of a particle a is computed as $c_a = \sqrt{\partial p / \partial \rho}$. We have found the use of artificial viscosity to have a minimal affect on the results in this paper, likely because significantly more viscosity is introduced through the constitutive law in the form of friction.

3.4 Boundary conditions

SPH ghost particles [28] are used to represent solid boundaries, as shown in Fig. 1b. The slip condition of interior particles past boundary particles can be tailored from a no-slip to a frictional-slip condition. In either case, boundary particles are given an artificial velocity when interacting

with interior particles to simulate a smooth velocity gradient across the boundary [13,28]. In particular, interior particle a will observe boundary particle b to have a velocity

$$\boldsymbol{v}_b = (1-\chi)\boldsymbol{v}_a + \chi \boldsymbol{v}_w, \tag{18}$$

where $\boldsymbol{v}_w$ is an imposed boundary velocity and $\chi = \min(\chi_{\max}, 1.0 + d_b/d_a)$. The value of $\chi_{\max}$ is set to 1.5, consistent with past work [13,28]. The lengths d_b and d_a are shown in Fig. 1b. This fictitious velocity for boundary particles b is used in all calculations of stress and strain rate at particle a.

To enforce a no-slip boundary condition, artificial stresses can be applied to boundary particles as described in [13,27] and used in [15]. In this case, an interior particle a will observe boundary particle b to have stress $\boldsymbol{\sigma}_b = \boldsymbol{\sigma}_a$ when the particles interact. To enforce a frictional-slip boundary condition, as is done throughout this paper unless otherwise noted, $\boldsymbol{\sigma}_b$ is merely computed using Eq. (2) with a boundary friction coefficient μ_b in the place of Eq. (11). In this way, interior particle a will observe boundary particle b to have a shear stress lower than that in the case of a no-slip boundary, thereby facilitating slip. In practice, this boundary friction coefficient may also be rate-dependent as illustrated in the examples below. To enforce a slip condition intermediate between no-slip and frictional-slip, $\boldsymbol{\sigma}_b$ can be set to a weighted average of $\boldsymbol{\sigma}_a$ and the value computed using Eq. (2).

The ρ_0 value for boundary particles is often set to a value of approximately 1 % below the that of interior particles to avoid penetration of interior particles into the boundary. An alternative approach, adopted in so-called XSPH, is to use a modified particle velocity [29]. However, the approach used here achieves the same objective without unnecessarily smoothing particle dynamics. In problems with higher relative velocities of two materials, XSPH may be necessary.

3.5 Time integration

We use a Velocity Verlet time integration scheme. This symplectic integrator has been shown to conserve momenta and energy, making it particularly attractive with SPH [22]. The basic approach involves computing an intermediate velocity

$$\boldsymbol{v}_a^{n+1/2} = \boldsymbol{v}_a^n + \frac{\boldsymbol{a}_a^n}{2}\Delta t, \tag{19}$$

where $\boldsymbol{a}_a^n$ is evaluated using $\boldsymbol{D}_a^n$ and $\boldsymbol{\sigma}_a^n$ computed with particle positions $\boldsymbol{x}_a^n$, where all superscripts represent time steps. SPH particle positions are updated by

$$\boldsymbol{x}_a^{n+1} = \boldsymbol{x}_a^n + \boldsymbol{v}_a^{n+1/2}\Delta t. \tag{20}$$

The final updated velocity at time step $n+1$ is computed by

$$\boldsymbol{v}_a^{n+1} = \boldsymbol{v}_a^{n+1/2} + \frac{\boldsymbol{a}_a^{n+1}}{2}\Delta t, \tag{21}$$

where $\boldsymbol{a}_a^{n+1}$ is evaluated using quantities $\boldsymbol{D}_a^{n+1}$ and $\boldsymbol{\sigma}_a^{n+1}$ computed with particle positions $\boldsymbol{x}_a^{n+1}$.

The time step Δt is chosen to satisfy a Courant condition, a limit imposed by maximal forces, and a viscous diffusion condition as discussed in [28,30]. These conditions amount to

$$\Delta t \leq \min\left(0.25\frac{h}{c_a}, 0.25\frac{h}{|\boldsymbol{f}_a|}, 0.125\frac{h^2\rho_a}{\mu_a p_a + c_a}\right), \tag{22}$$

where the last condition emerges from the viscous condition discussed in [28,30]. Some trial-and-error may be necessary to ensure satisfaction of the second condition of Eq. (22).

4 Examples

This section illustrates three examples of the constitutive law and numerical method described above. The first example demonstrates the ability of the rate-dependent friction coefficient to produce non-zero flow profiles at various inclination angles. The second example illustrates that the constitutive law and numerical method produce column collapse runout and height scaling consistent with experiments. The third example demonstrates that the constitutive law and numerical method accurately capture the transient profiles of column collapses down inclined planes. This range of problems involves a variety of flow rates, highlighting the versatility of the proposed modeling framework and suggests its viability for modeling the full evolution of geophysical flows. All simulations are performed twice, once with dilation, β, included in the friction coefficient ($\mu = \mu_{ss} + \beta$) and once with dilation excluded ($\mu = \mu_{ss}$), illustrating how this term influences our results.

4.1 Example 1: infinite inclined plane flow

Inclined plane flows are a classical test of granular media's flow rheology. Experiments in this flow configuration have been used to derive rate-dependent frictional parameters [5], study Bagnold-type velocity profiles, investigate boundary slip, and examine non-local and finite-size effects [4,31]. An essential feature of dry granular materials flowing down inclined planes is their ability to reach a steady-state velocity profile for a range of inclination angles. This characteristic is the signature of rate-dependent steady-state friction and distinguishes the liquid-like flow regime of granular media from Newtonian rate-independent fluids. In this example,

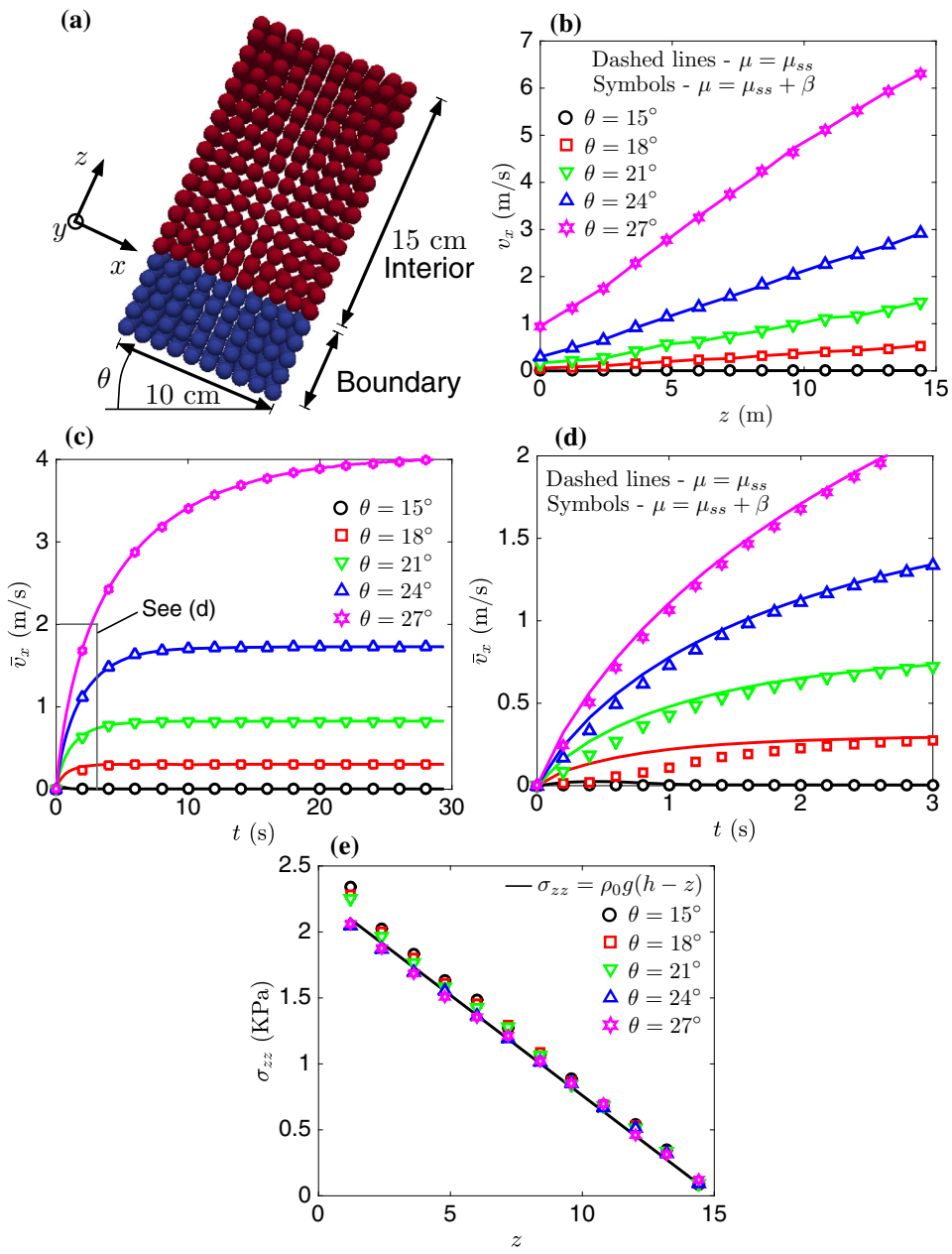

Fig. 2 **a** Initial geometry of the infinite inclined plane flow simulations showing SPH particles representing the granular material overlaying SPH boundary particles. **b** Steady-state profiles for inclination angles $\theta = 15°$ through $\theta = 27°$. **c** Mean velocities illustrating the approach to steady-state. **d** Mean velocities at the onset of flow. **e** Pressure as a function of depth at $t = 30$ s

we test the ability of our constitutive framework to produce a steady-state velocity profile for a range of inclination angles.

The geometry of the inclined plane flow simulations is shown in Fig. 2a. A bulk of granular material measuring 10 cm in the x dimension, 15 cm in the z dimension, and 5 cm in the y dimension is modeled with periodic boundaries in the x and y dimensions. The total number of SPH particles is 750 in the interior of the flow and 250 in the boundary. We have found this number sufficient to provide smooth continuum fields. Despite being small, this number does not reduce the number of particles in the support domain of a single particle below that which is typical for evaluating functions and their derivatives [22]. The material and boundary are rate-dependent with $\mu_l = 0.268$ ($\phi = 15°$), $\mu_h = 0.557$ ($\phi = 30°$), and $D^* = 15\,\mathrm{s}^{-1}$. Other parameters are listed in Table 1. Inclination angles from $\theta = 12°$ through $\theta = 33°$ in increments of 3° are simulated by rotating the gravity field with respect to the global coordinate frame at time $t = 0$s.

Table 1 Model parameters used in infinite inclined plane flow simulation

ρ_0 (kg/m^3)	μ_l	μ_h	D^* (s^{-1})	c (Pa)	μ_b	κ (Pa)	γ	Δx (m)
1550	0.268	0.557	15	0	μ	10^5	1.5	0.01

Steady-state flow velocities, obtained by averaging SPH particle velocities binned at various heights and extrapolating as necessary to $z = 0$, are shown in Fig. 2b for simulations using $\theta = 15°$ through $\theta = 27°$. Solid lines represent simulations with $\mu = \mu_{ss}$ and symbols represent simulations with $\mu = \mu_{ss} + \beta$. These two types of simulation give nearly identical results at steady-state, as expected. Only inclination angles $15° < \theta \leq 30°$ result in non-zero steady-state flow profiles. Results for $\theta = 15°$ are shown to illustrate that there is no flow (to machine precision) unless $\theta > \tan^{-1}(\mu_s)$. Results for $\theta = 30°$ approach a steady-state but over very long times and are therefore not shown. Results for $\theta > 30°$ do not approach a steady-state but experience unbounded particle acceleration with time. It is clear that the constitutive law and numerical method capture the ability of rate-dependent granular materials to reach a steady-state velocity profile for a range of inclination angles.

Flow profiles in Fig. 2b appear to be nearly linear except for slight deviations at the boundary and at the free surface. The non-zero velocity gradient at the free surface is consistent with experimental findings (see [4] and references therein). We do not expect Bagnold velocity profile in the current work since Eq. (9) relates μ_{ss} to $|\boldsymbol{D}|$ rather than the inertial number I [4]. Extending Eq. (9) to relate μ_{ss} to I and examining of how this changes the precise shape of the flow profile is reserved for future work. Flow profiles also notably display boundary slip. We have verified that boundary slip is nearly eliminated by using a no-slip, rather than a frictional-slip, condition, as described in Sect. 3.4.

Figure 2c illustrates the mean velocity $\bar{v}_x$ of all SPH particles in the flow direction as a function of time. All results for $\theta \leq 30°$ approach a constant mean velocity. Figure 2d illustrates the same results at the beginning of the simulation. It can be observed that simulations employing dilation in the friction coefficient ($\mu = \mu_{ss} + \beta$) exhibit lower velocities at the onset of flow. This partial suppression of initial particle acceleration is expected: any volumetric expansion caused by initial motion will increase μ, thus decreasing the flow rate. At later times, simulations both with and without dilation are in excellent agreement. The time at which simulations come into excellent agreement is a function of both inclination angle and the parameter η in Eq. (10).

Figure 2e illustrates the vertical pressure σ_{zz} at steady-state ($t = 30\,\text{s}$) compared with the analytical curve $\sigma_{zz} = \rho_0 g(h - z)$. For clarity, only simulations with $\mu = \mu_{ss} + \beta$ are shown in symbols. Simulations with $\mu = \mu_{ss}$ exhibit nearly identical results. The simulations show a monotonic vertical pressure increase with depth in close agreement with the analytical curve. The observed deviations are expected: overburden pressure will cause $\rho > \rho_0$ and the rotated gravity field will cause lower g_z as inclination angle is increased.

4.2 Example 2: column collapse scaling

4.2.1 Scaling laws

An important test geometry for the flow of granular materials is the collapse of a granular column on a flat surface. This test establishes the relationship between the initial aspect ratio of the column, $a = H_0/L_0$, and final runout and slumped height, usually in the form of scaling laws such as

$$\frac{H_0}{H} \sim \lambda_1 a^{\alpha_1} \quad \text{and} \quad \frac{L - L_0}{L_0} \sim \lambda_2 a^{\alpha_2}, \tag{23}$$

where $\lambda_1, \lambda_2, \alpha_1$, and α_2 are constants [10,11,32–38]. To accurately predict the dynamics of processes such as landslides, granular avalanches, and dam-break scenarios, any model for granular materials should, as a first test, be able to produce scaling laws that are consistent with experimental findings. In this example, we test our model's ability to accurately produce such scaling laws by modeling column collapses on flat surfaces and comparing the scaling laws with experimental findings from [32].

The geometries of column collapse simulations are shown in Fig. 3. We use two geometries, reflecting the grit (sand) and glass bead experiments reported in [32]. The grit, shown in Fig. 3a, is confined to a 9 cm by 10 cm (into the page) chamber. Initial heights H_0 vary and employ anywhere from 400 to 12,000 interior SPH particles. These conditions reflect the "wide slot" experiments on grit reported in [32], except that our simulations use half their width and instead employs periodic boundary conditions (into the page) to capture the quasi-two-dimensionality of the test. The glass bead specimen is confined to a 2.5 cm by 10 cm

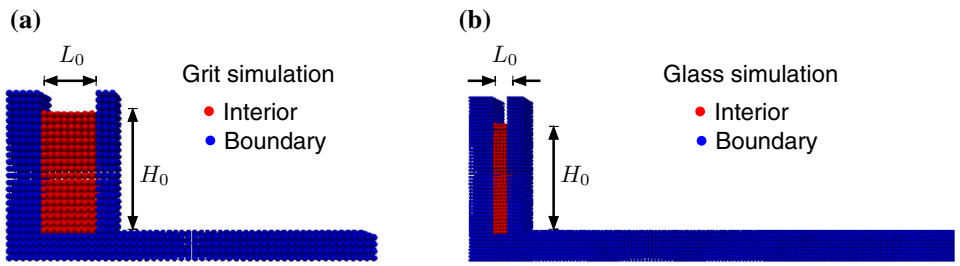

Fig. 3 Initial geometry of **a** grit (sand) and **b** glass bead simulations. These geometries reflect those of [32] for the compared results

Table 2 Model parameters used in the column collapse simulations

Material	ρ_0 (kg/m^3)	μ_l	μ_h	D^* (s^{-1})	c (Pa)	μ_b	κ (Pa)	γ	Δx (m)
Grit	1404	0.74	0.74	–	0	0.335	10^5	1.5	0.01
Glass	1450	0.456	0.456	–	0	0.263	10^5	1.5	0.005

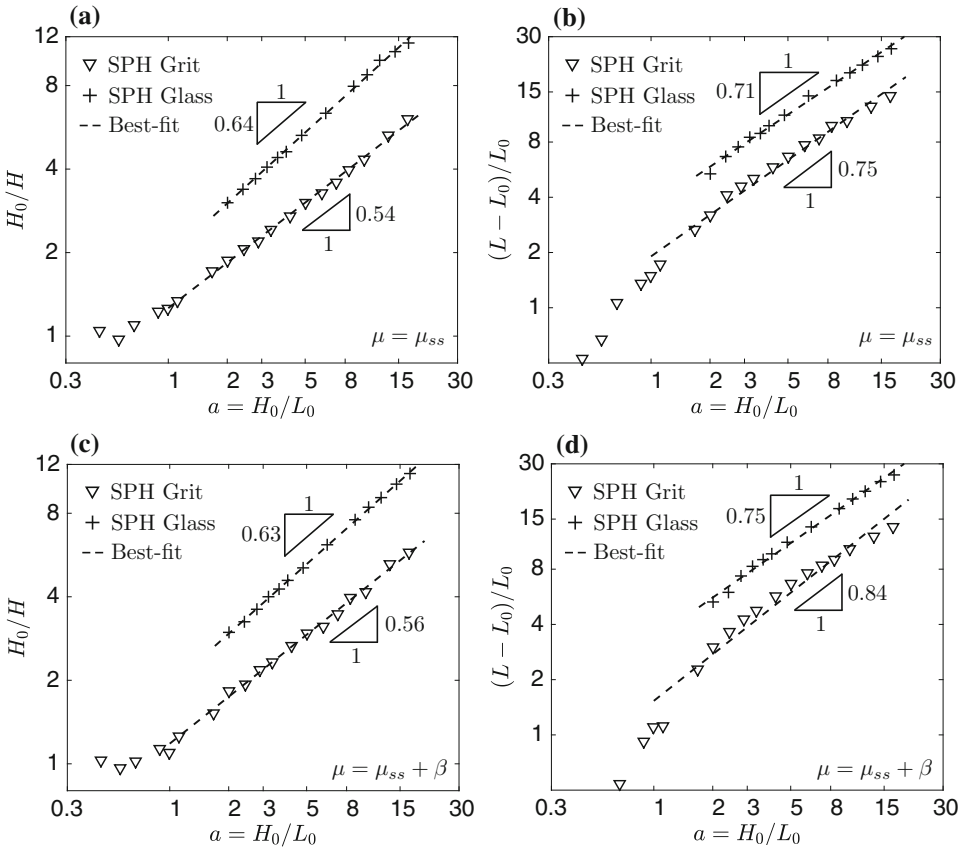

Fig. 4 Simulated column collapse scaling and best-fit lines to Eq. (23) for simulations excluding β in μ (**a**, **b**) and simulations including β in μ (**c**, **d**)

chamber and also has variable initial heights H_0 employing anywhere from 800 to 1600 interior SPH particles. These conditions also reflect the "wide slot" experiments on glass beads reported in [32]. All other material properties are described in Table 2. The grit and glass possess distinct loose-packed densities, internal friction coefficients, and basal friction coefficients, further challenging our constitutive law with a variety of materials and substrates. We model the glass with a finer particle spacing $\Delta x = 0.005$ m since these materials are confined to an initially thinner slot than the grit.

Figure 4a, b illustrates slumping and runout scaling, respectively, for simulations using $\mu = \mu_{ss}$ and Fig. 4c, d illustrates the scaling for simulations using $\mu = \mu_{ss} + \beta$. All scaling exponents are found by a least-squares fit of a linear line to the data in logarithmic space. Only data with $a \geq 1$ are used for fitting for comparison with [32] (see Fig. 11 of that reference). Table 3 further compares the scaling exponents α_1 and α_2 (values of λ_1 and λ_2 are not reported by [32] but are said to be material-dependent).

Table 3 Scaling parameters found in column collapse simulations

Source	α_1	α_2
SPH grit ($\mu = \mu_{ss}$)	0.54	0.75
SPH glass ($\mu = \mu_{ss}$)	0.64	0.71
SPH grit ($\mu = \mu_{ss} + \beta$)	0.56	0.84
SPH glass ($\mu = \mu_{ss} + \beta$)	0.63	0.75
[32] Grit	0.6	0.9 ± 0.1
[32] Glass	0.6	0.9 ± 0.1

The scaling laws found in all simulations closely agree with experimental results of [32]. The observed deviation is expected since boundary and initial conditions may not be perfectly reproduced in the simulations. All simulations including β in μ agree slightly better with experimental findings than those excluding it. This agreement demonstrates that the current modeling framework accurately captures the scaling behavior of granular column collapses, thus making it attractive for modeling the evolution of geophysical

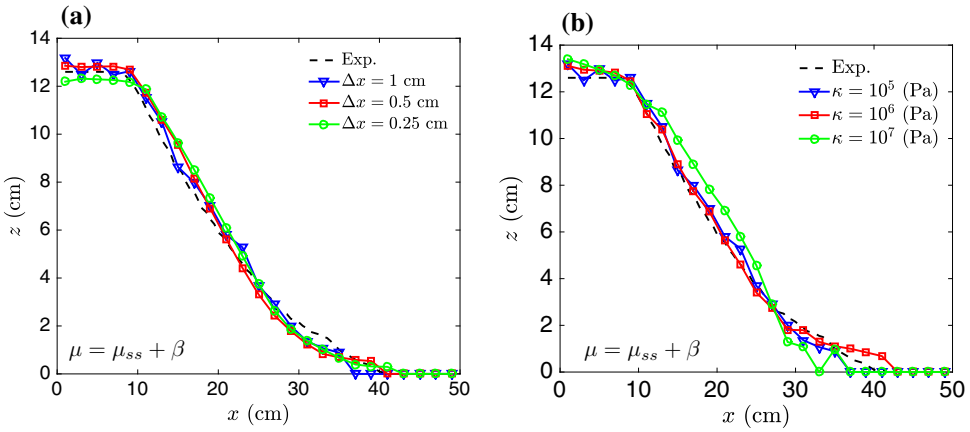

Fig. 5 **a** Column collapse profiles with resolution refinement. **b** Column collapse profiles using a bulk modulus varied over two orders of magnitude. The reduced bulk modulus matches experimental results as well as the largest bulk modulus

processes such as landslides and granular avalanches. In Sec. 4.3 we explore this claim further by comparing non-steady dynamics of a collapse process with experimental results.

4.2.2 Parametric study

Here, we briefly examine the sensitivity of the results of a typical column collapse simulation to changes in bulk modulus and SPH resolution. The purpose of these simulations is to establish (1) the accuracy (for certain problems) of using a reduced bulk modulus to reduce computation time; (2) the influence of resolution refinement on convergence of simulation results. We choose to test model sensitivity with a column collapse simulation because column collapse has been established above as a challenging test of the granular flow rheology. All simulations use the grit properties reported in Table 2 to model a column collapse with initial geometry of 20 cm in the x dimension, initial height of 13 cm in the z direction, and a width of 18 cm in the y direction (modeled with periodic boundaries). We choose these particular inputs because experimental results for collapsed column profiles are available in [32] (see Fig. 12 of that publication; their H_0 is 12.7 cm rather than 13 cm).

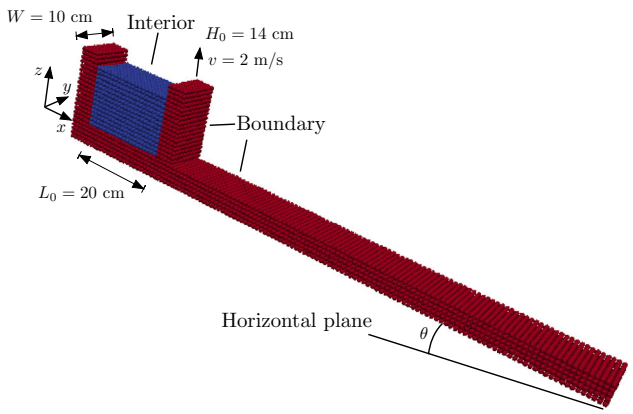

Fig. 6 Initial geometry of column collapses down inclined planes. Sidewalls from [39] are modeled but not shown

Figure 5a illustrates results for varying initial particle spacing (and mass accordingly to ensure initial conditions of $\rho = \rho_0$) while holding other parameters from Table 2 fixed. The finest resolution uses 299,520 interior SPH particles and the coarsest resolution uses 4680 interior SPH particles. Since resolution is a function of particle mass in SPH simulations of continua, this is equivalent to a mesh convergence test. Fig. 5a illustrates that progressive refinements in resolution yield collapse profiles agreeing with experimental results from [32]. The coarsest resolution uses the same particle spacing employed in other examples in this paper and provides nearly identical results to the finest resolution.

Figure 5b illustrates results for varying the bulk modulus in simulations. The bulk modulus used for examples throughout this paper employs $\kappa = 10^5$ (see Eq. 4), making it artificially low with the benefit of permitting larger time steps and faster computation time. As shown in Fig. 5b, decreasing the bulk modulus two orders of magnitude from this artificially low value does not improve or significantly change results in this simulation, validating this choice. Similar tests have been applied to the other examples presented in this paper. We therefore believe that using an artificially low bulk

Table 4 Model parameters used in the study of flow dynamics down inclined planes

Simulation	ρ_0 (kg/m^3)	μ_l	μ_h	D^* (s^{-1})	c (Pa)	μ_b	κ (Pa)	γ	Δx (m)
S1	1550	0.435	μ_l	–	0	0.18	10^5	1.5	0.01
S2	1550	0.435	μ_l	–	0	0.18	10^5	1.5	0.01
S3	1550	0.435	0.68	15	0	0.18	10^5	1.5	0.01

modulus can improve computation time without sacrificing accuracy in problems where neither wave speed nor quasi-static stiffness dominates the results. More research is needed to determine a rigorous criterion for artificially reducing the bulk modulus, which may benefit many numerical methods beyond those discussed in this paper.

4.3 Example 3: dynamics of flow down inclined planes

Granular flows down inclined planes reach higher velocities and strain rates than those on flat surfaces [20] and are therefore a more challenging test of a modeling framework's ability to capture a wide range of flow-rate regimes.

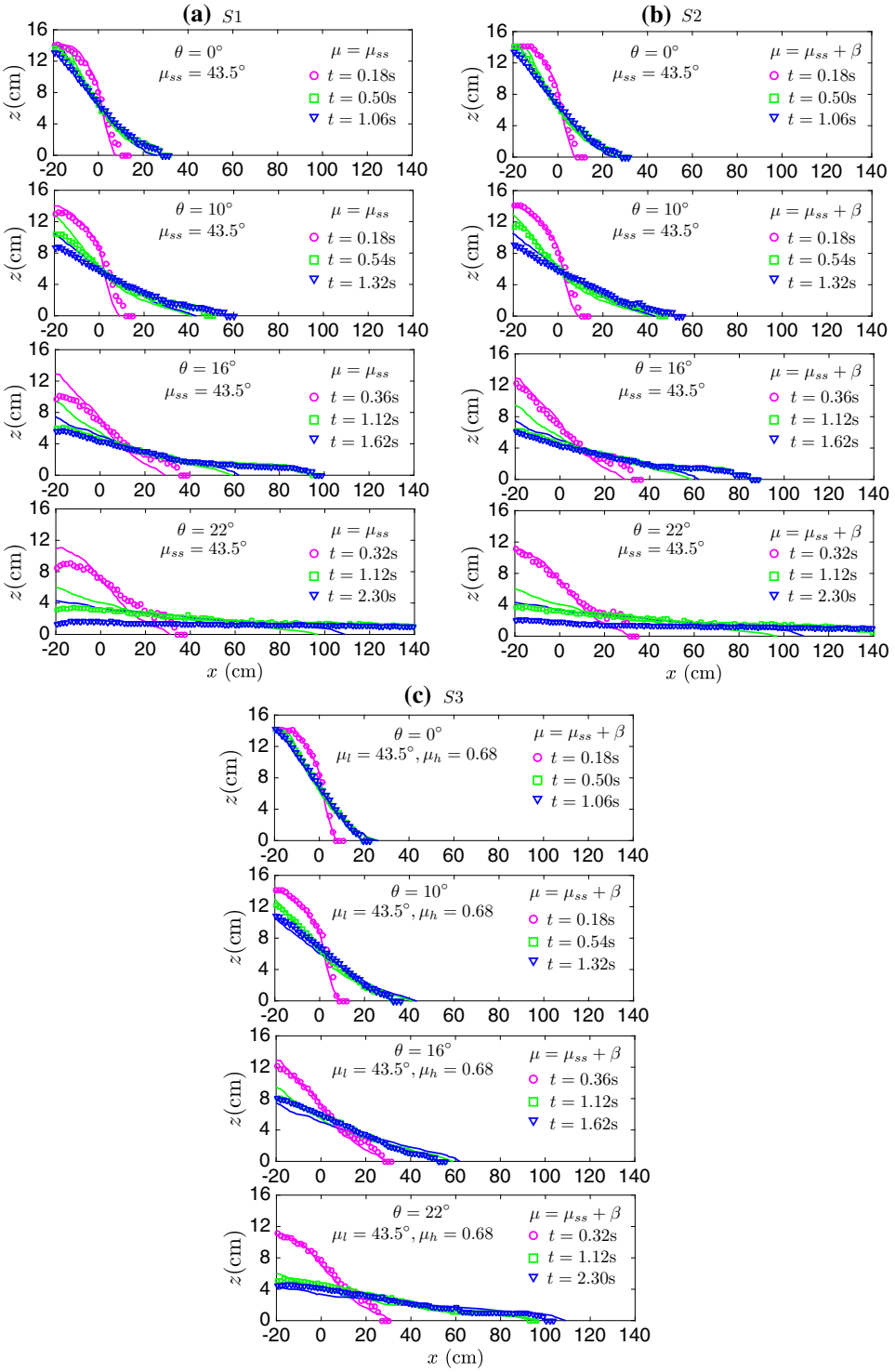

Fig. 7 A comparison of the dynamic profiles of column collapses between SPH simulations (*symbols*) and experimental results of [39] (*lines*). For clarity, *three symbols*, spaced 0.01 cm apart, are plotted at $z = 0$cm beyond the farthest extent of SPH particles. **a** Results for SPH simulations S1 excluding β from μ with rate-independent μ_{ss}. **b** Results for SPH simulations S2 including β in μ with rate-independent μ_{ss}. **c** Results for SPH simulations S3 including β in μ with rate-strengthening μ_{ss}

Numerical methods such as DEM can typically reproduce scaling laws like those discussed in Sec. 4.2 but overestimate the non-steady slumping rate and final runout of individual collapse experiments [36]. To illustrate that our proposed method accurately models these challenging flow environments, this example compares non-steady granular column collapse profiles with those reported in [39].

We simulate glass beads in the initial geometry shown in Fig. 6 for four inclination angles: $\theta = 0°, 10°, 16°$, and $22°$. The granular material is initially confined in an area measuring 20 cm in the x dimension and 10 cm in the y dimension, with an initial height of 14 cm. A total of 2800 interior SPH particles are included in each simulation. The sidewalls present in experiments are also explicitly modeled but are omitted from the rendering for clarity. The simulated material has $\mu_s = \tan(23.5°)$, where $23.5°$ is the internal friction angle reported in [39]. Three simulations are performed to underscore how dilation rate and rate-dependent friction affect the results: (1) simulations S1 (see Table 4) using $\mu = \mu_{ss}$ with rate-independent friction; (2) simulations S2 using $\mu = \mu_{ss} + \beta$ with rate-independent friction; (3) simulations S3 using $\mu = \mu_{ss} + \beta$ with rate-dependent friction. Other model inputs are the same for all tests, as reported in Table 4. All simulations use 2800 interior SPH particles. The friction parameters used in simulations S3 for the granular material reflect the average of those reported in [5,16] for the same material. Simulations S3 also employ rate-strengthening parameters for the basal friction coefficient ($\mu_{bs} = 0.18$, $\mu_{bh} = 43$, and $D^* = 15\,\mathrm{s}^{-1}$). For each simulation, the wall restraining particle motion is moved upward at 2 m/s starting at $t = 0$ s to mimic experimental conditions of [39].

Column collapse profiles are obtained by examining the spatial extent of SPH particles in the $x - z$ plane at various times. Figure 7 compares profiles obtained from SPH simulations (symbols) with those reported in [39] (lines) at three times during each collapse. For S1 (Fig. 7a) where dilation and rate-dependence are omitted, simulations agree with experiments reasonably well at low inclination angles but fail to match experiments at higher inclination angles. Most notably, simulations S1 exhibit excessive slumping at the left wall and over-predict runout. These deficiencies are the same as those found by [16] using a similar viscoplastic constitutive law in a finite-element framework.

Simulations S2 correct the excessive slumping problem, particularly at early times, and reduce runout predictions, suggesting that including β in the calculation of μ improves early-time predictions of dynamics. However, at the highest inclination angles, simulations S2 continue to exhibit excessive slumping and runout. Simulations S3 illustrate an excellent agreement for slumping and runout in all simulations. This remarkable agreement suggests that including dilatancy and rate-dependence in the constitutive law is necessary for modeling flow-rate regimes experienced by columns collapsing down inclined planes. The close agreement with experimental results also suggests that the method, when properly calibrated, may be able to predict the full time-dependent dynamics of geophysical events such as landslides and avalanches, as well as similar industrial flows.

In light of these results, we suggest that the proposed framework may also be used in the future to investigate the 3D pressure and velocity fields responsible for the observed behaviors of granular flows. For instance, the framework may shed light on the dynamics of avalanches over realistic terrains, the basal pressures exerted by landslides on underlying soils (and their frequency spectrum), and the pressures exerted within containing vessels during filling or transport. We leave a thorough investigation of such phenomena for future work.

5 Discussion and conclusion

To conclude, we have presented a constitutive law and modeling framework for simulating the rate-dependent behavior of granular flows. The proposed constitutive law captures the steady-state and transient behavior of granular flows by linking friction to strain rate and dilation. We have notably demonstrated the ability of the constitutive law to capture the transient profiles of a collapsing 3D granular column as well as scaling laws for final heights and lengths. The SPH implementation makes modeling arbitrarily large deformations simple and efficient. The framework may be used in the future to study three-dimensional continuum fields in geophysical and industrial granular flows.

Future work may address possible shortcomings of the proposed constitutive law and numerical method. In particular, a more reliable approach for achieving oscillation-free pressure fields can be explored [27]. This will enable Eq. (9) to employ I rather than $\boldsymbol{D}$ for consistency with a broader class of problems. Future work can also provide a more systematic calibration of parameters, such as η in Eq. (10) or D^* in Eq. (9), to numerical or experimental results. This will enable accurate modeling of geophysical and industrial events with a variety of materials and substrates.

Acknowledgements Support by the Air Force Office of Scientific Research Grant # FA9550-12-1-0091 through the University Center of Excellence in High-Rate Deformation Physics of Heterogeneous Materials is gratefully acknowledged. This work was partially performed under the auspices of the U.S. Department of Energy by Lawrence Livermore National Laboratory under Contract DE-AC52-07NA27344.

References

1. Jaeger HM, Nagel SR, Behringer RP (1996) Granular solids, liquids, and gases. Rev Mod Phys 68(4):1259

2. Savage SB, Sayed M (1984) Stresses developed by dry cohesionless granular materials sheared in an annular shear cell. J Fluid Mech 142:391–430
3. Campbell CS (1990) Rapid granular flows. Annu Rev Fluid Mech 22(1):57–90
4. MiDi GDR (2004) On dense granular flows. Eur Phys J E 14(4):341–365
5. Jop P, Forterre Y, Pouliquen O (2006) A constitutive law for dense granular flows. Nature 441(7094):727–730
6. Wood DM (1990) Soil behaviour and critical state soil mechanics. Cambridge University Press, Cambridge
7. Andrade JE, Chen Q, Le PH, Avila CF, Evans TM (2012) On the rheology of dilative granular media: bridging solid-and fluid-like behavior. J Mech Phys Solids 60(6):1122–1136
8. Forterre Y, Pouliquen O (2008) Flows of dense granular media. Annu Rev Fluid Mech 40:1–24
9. Jutzi M, Asphaug E (2011) Forming the lunar farside highlands by accretion of a companion moon. Nature 476(7358):69–72
10. Lacaze L, Kerswell RR (2009) Axisymmetric granular collapse: a transient 3d flow test of viscoplasticity. Phys Rev Lett 102(10):108305
11. Mast CM, Arduino P, Mackenzie-Helnwein P, Miller GR (2014) Simulating granular column collapse using the material point method. Acta Geotech 10(1):101–116
12. Dunatunga S, Kamrin K (2015) Continuum modelling and simulation of granular flows through their many phases. J Fluid Mech 779:483–513
13. Bui HH, Fukagawa R, Sako K, Ohno S (2008) Lagrangian meshfree particles method (SPH) for large deformation and failure flows of geomaterial using elastic-plastic soil constitutive model. Int J Numer Anal Methods Geomech 32(12):1537
14. Chen W, Qiu T (2011) Numerical simulations for large deformation of granular materials using smoothed particle hydrodynamics method. Int J Geomech 12(2):127–135
15. Minatti L, Paris E (2015) A sph model for the simulation of free surface granular flows in a dense regime. Appl Math Model 39(1):363–382
16. Ionescu IR, Mangeney A, Bouchut F, Roche O (2015) Viscoplastic modeling of granular column collapse with pressure-dependent rheology. J Non-Newton Fluid Mech 219:1–18
17. Monaghan JJ (1994) Simulating free surface flows with sph. J Comput Phys 110(2):399–406
18. Zhang HP, Makse HA (2005) Jamming transition in emulsions and granular materials. Phys Rev E 72(1):011301
19. Hurley RC, Andrade JE (2015) Strength of granular materials in transient and steady state rapid shear. Proc Eng 103:237–245
20. Lucas A, Mangeney A, Ampuero JP (2014) Frictional velocity-weakening in landslides on earth and on other planetary bodies. Nat Commun 5:3417
21. Bolton MD (1986) The strength and dilatancy of sands. Geotechnique 36(1):65–78
22. Monaghan JJ (2005) Smoothed particle hydrodynamics. Rep Prog Phys 68(8):1703
23. Monaghan JJ, Lattanzio JC (1985) A refined particle method for astrophysical problems. Astron Astrophys 149:135–143
24. Price DJ, Monaghan JJ (2004) Smoothed particle magnetohydrodynamics-II. Variational principles and variable smoothing-length terms. Mon Not R Astron Soc 348(1):139–152
25. Liu MB, Liu GR (2010) Smoothed particle hydrodynamics (SPH): an overview and recent developments. Arch Comput Methods Eng 17(1):25–76
26. Plimpton S, Crozier P, Thompson A (2007) LAMMPS-large-scale atomic/molecular massively parallel simulator. Sandia Natl Lab 18:27–41
27. Randles PW, Libersky LD (1996) Smoothed particle hydrodynamics: some recent improvements and applications. Comput Methods Appl Mech Eng 139(1):375–408
28. Morris JP, Fox PJ, Zhu Y (1997) Modeling low Reynolds number incompressible flows using sph. J Comput Phys 136(1):214–226
29. Monaghan JJ (1989) On the problem of penetration in particle methods. J Comput Phys 82(1):1–15
30. Monaghan JJ (1992) Smoothed particle hydrodynamics. Annu Rev Astron Astrophys 30:543–574
31. Silbert LE, Ertaş D, Grest GS, Halsey TC, Levine D, Plimpton SJ (2001) Granular flow down an inclined plane: bagnold scaling and rheology. Phys Rev E 64(5):051302
32. Balmforth NJ, Kerswell RR (2005) Granular collapse in two dimensions. J Fluid Mech 538:399–428
33. Lube G, Huppert HE, Sparks RSJ, Hallworth MA (2004) Axisymmetric collapses of granular columns. J Fluid Mech 508:175–199
34. Lube G, Huppert HE, Sparks RSJ, Freundt A (2005) Collapses of two-dimensional granular columns. Phys Rev E 72(4):041301
35. Kerswell RR (2005) Dam break with coulomb friction: a model for granular slumping? Phys Fluids (1994-present) 17(5):057101
36. Staron L, Hinch EJ (2005) Study of the collapse of granular columns using two-dimensional discrete-grain simulation. J Fluid Mech 545:1–27
37. Lagrée P-Y, Staron L, Popinet S (2011) The granular column collapse as a continuum: validity of a two-dimensional Navier–Stokes model with a μ (i)-rheology. J Fluid Mech 686:378–408
38. Farin M, Mangeney A, Roche O (2014) Fundamental changes of granular flow dynamics, deposition, and erosion processes at high slope angles: Insights from laboratory experiments. J Geophys Res 119(3):504–532
39. Mangeney A, Roche O, Hungr O, Mangold N, Faccanoni G, Lucas A (2010) Erosion and mobility in granular collapse over sloping beds. J Geophys Res(2003–2012) 115(F3):30